

Received: 6 August 2018 Accepted: 17 December 2018 Published online: 04 February 2019

# **OPEN** Cyclability evaluation on Si based **Negative Electrode in Lithium** ion Battery by Graphite Phase Evolution: an operando X-ray diffraction study

Chih-Wei Hu1, Jyh-Pin Chou2, Shang-Chieh Hou3, Alice Hu62, Yu-Fan Su4, Tsan-Yao Chen1,5, Wing-Keong Liew<sup>4</sup>, Yen-Fa Liao<sup>6</sup>, Jow-Lay Huang<sup>3,5</sup>, Jin-Ming Chen<sup>6</sup> & Chia-Chin Chang<sup>6</sup>

Artificial graphite (FSN) additive is employed as internal structural label for projecting cyclability of Si material native electrode in a mass ratio of Si/FSN = 1.0 in Li ion battery (LIB). Results of operando X-ray diffraction analysis on Si-FSN negative electrode in LIB demonstrate that one can evaluate the lithiation and delithiation affinity of active material by referring phase transition delay of graphite as affected by experimental splits in a formation process of LIB. We prove that a thin layer of surface amorphous structure and residual lattice strain are formed in Si by high energy ball-milling treatment. Those manipulations improve Li intercalation kinetics and thus enabling a capacity fading of less than 10% (from 1860 to 1650 mAhq<sup>-1</sup>) for Si negative electrode in 50 cycles. Of utmost importance, this study discloses a robust assessment for revealing mechanism on amorphous and strain related silicide formation and predicting cyclability of negative electrode by quantitative phase evolution rate of FSN additive in LIB.

With raising demand of power consumption in transportation platforms, portable electronics, as well as high energy density modulation and storage system, high capacity materials are evitable issues for development of Li ion battery (LIB). With such a consideration, silicon based materials are no doubt the next generation negative electrode material in LIB due to its highest theoretical capacity among studied materials<sup>1,2</sup>. However, as compared to existing negative electrode materials, the lithium diffusion coefficient and intrinsic conductivity of Si are relatively low hindering its steps into the market<sup>3</sup>. Furthermore, Si possesses a volume expansion up to 400% due to a solid-state alloying reaction in lithiation (charge) process<sup>4</sup>. It induces extensive stress between residual Si and Li interacted domain, therefore, leading to pulverization of silicon powder in negative electrode and instability of the solid electrolyte interphase (SEI) layer<sup>5,6</sup>. Those characteristics pill off Si powders from current collector and increase electrical contact resistance in electrode<sup>7-9</sup>. Meanwhile, crashed Si powders exposes fresh surface to electrolyte thus causing overgrowth of solid electrolyte interface (ESI). In past decades, improvements in the cyclability and rate capability of silicon negative electrodes have been demonstrated by reducing particle size to the nanoscale<sup>10</sup>, seeking conductive coatings<sup>11</sup> or conductive networks<sup>12</sup>, providing void space to accommodate volume expansion<sup>13</sup>, and introducing highly elastic phases to mitigate the deleterious effect of large volume changes<sup>14,15</sup>. Regardless of attempts been utilized, cyclability of LIB has been partially improved and is still far from criteria of the commercialization.

<sup>1</sup>Department of Engineering and System Science, National Tsing Hua University, Hsinchu, 30013, Taiwan. <sup>2</sup>Department of mechanical and biomedical engineering, City University of Hong Kong, Kowloon, Hong Kong SAR. <sup>3</sup>Department of Materials Science and Engineering, National Cheng Kung University, Tainan, 70101, Taiwan. <sup>4</sup>Department of Greenergy, National University of Tainan, Tainan, 70005, Taiwan. ⁵Hierarchical Green-Energy Materials (Hi-GEM) Research Center, National Cheng Kung University, Tainan, 70101, Taiwan. 6 National Synchrotron Radiation Research Center, Hsinchu, 30076, Taiwan. Correspondence and requests for materials should be addressed to T.-Y.C. (email: chencaeser@gmail.com) or C.-C.C. (email: ccchang@mail.nutn.edu.tw)

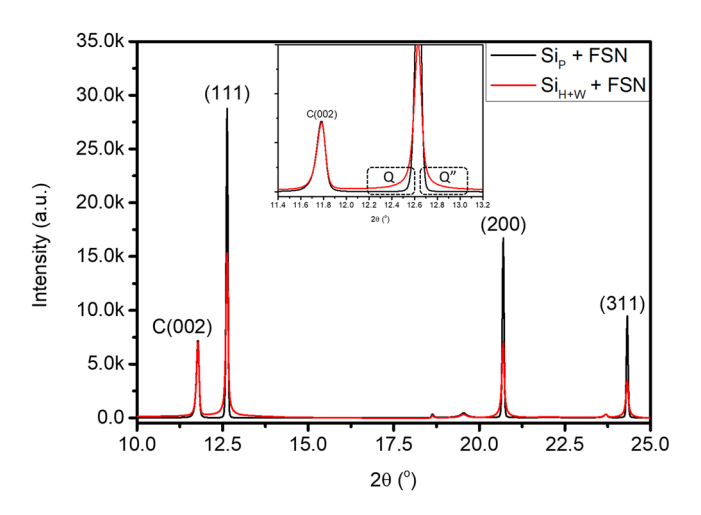


**Figure 1.** XRD patterns of as-prepared  $Si_P + FSN$  and  $Si_{H+W} + FSN$  electrodes. Inset presents room in for the two diffraction patterns in a range from 11.4° to 13.2°. Wavelength of incident X-ray is 0.689 Å (18 keV).

With safety and cost considerations, capacity, failure mode, and cyclability are essential inspections for commercialization of LIB. In these inspections, cyclability takes the longest time and largest resources, therefore, are long-standing issue for the slow development of LIB. Internal standard could be an efficient label as comparison for redox responses of active materials in electrochemical devices. Such a technique is conventionally employed by adding stable materials with known structure and chemical state in target sample for calibrating spatial or chemical specifications upon physical inspections (including X-ray absorption spectroscopy (XAS), X-ray diffraction (XRD), and X-ray photoemission (XPS)) and process development in semiconductor. However, internal standard is rarely being used due to the insufficient information on kinetics of structural evolutions for active materials operando LIB devices. In this study, artificial conducting graphite (FSN) is employed as internal structural label for verifying lithiation and delithiation affinity of active materials operando LIB. By cross-referencing results of density functional theory (DFT) calculation and operando XRD, effects of high energy milling on silicide formation and lithiation/delithiation affinity of Si materials are quantitatively revealed by changes of crystal structure of FSN as a function of applied potential of LIB. Notice that, priority of phase evolution between Si and graphite domains are dominated by their affinity to lithiation. Consequently, obtained results not only disclose the Li ion insertion/extraction behaviours in negative electrode but provide a new class of internal standard method for projecting quality and cyclability of silicon-based materials in formation stage of LIB.

#### **Results and Discussion**

Physical Structure Characterizations on Si based materials. Crystal structure of  $Si_P$  and  $Si_{H+W}$  is revealed by using XRD analysis. Structure parameters are quantitatively determined by Rietveld refinement on their diffraction patterns (Fig. S1) and corresponding lattice parameters of  $Si_P + FSN$  and  $Si_{H+W} + FSN$  are listed in Table S1. Accordingly, lattice parameter is 5.435(6) Å and unit cell volume (V) is 160.598(9) Å<sup>3</sup> for Si<sub>H+W</sub>. For Si<sub>B</sub>, lattice constant is 5.431(3) Å and unit cell volume is 160.218(0) Å<sup>3</sup>. As a result, one can notice a slight distortion and lattice expansion by 0.24% on Si crystal ( $Si_{H+W}$ ) by high energy ball-milling treatment. Diffraction patterns of the two electrode are compared in Fig. 1 and intensity is normalized by that of FSN (002) peak. Accordingly, all diffraction peaks of Si<sub>H+W</sub> + FSN possess lower intensity, broader peak width accompanied with stronger diffusion scattering background (denoted by Q and Q" in inset) as compared to those of  $Si_p + FSN$ . As consistently proved by high resolution transmission electron microscopy (HRTEM) images in Fig. S2 and XRD analysis (Table 1), those characteristics can be ascribed for formation of amorphous Si species, certain short range disorder structure (sub-nanometer domains), and increased preferential (111) facets in Si<sub>H+W</sub> by HEMM. Quantitative structural parameters are summarized in Table 1. Accordingly, crystal structure of Si phase remaining unchanged by HEMM treatment. For  $Si_P + FSN$ , average coherent length ( $D_{avg}$ ) is 834.9 Å for (111), 790.5 Å for (220), and 757.1 Å for (311) facets in Si phase. After HEMM treatments,  $D_{avg}$  of  $\check{Si}_{H+W}+FSN$  is respectively. tively reduced by 20% in (111) facet (624.2 Å), ~43% in (220) facet (451.7 Å), and 46% in (311) facet (455.4 Å) as compared to those of  $Si_P + FSN$ . In a meantime,  $H_{(111)}/H_{(220)}$  and  $H_{(111)}/H_{(311)}$  is respectively increased to 2.215 and 4.493 revealing its significant preference along Si (111) facet as compared to that of ideal Si crystal and Sip Changes of those parameters resembles the "damage" of Si phase by high energy treatment and thus increasing the asymmetric crystal ratio in (111) facet.

Interface Properties of Experimental Si based Negative Electrode Materials by DFT calculation and ElS characterization. Affinity of Li silicide formation is a crucial factor in performance of Si materials as negative electrode in LIB. This factor is a combination results including atomic packing density of facets, size of Si crystal, and anchoring ligands as dock for Li intercalation. Effects of proposed high energy milling treatment on Li silicide formation affinity are evidenced by cross-referencing DFT (with structure models determined by XRD fitting) and XRD determined crystal structure evolution of experimental materials in *operando* LIB. Figure 2 compares top view of DFT calculated atomic packing structure for models of Li<sub>15</sub>Si<sub>4</sub> clusters in Si

Sample	Facet	2θ	D <sub>avg</sub> (Å)	d (Å)	H <sub>(111)</sub> /H <sub>(hkl)</sub> **
$Si_p + FSN$	(002)*	11.787	445.4	3.355	
	(111)	12.634	780.2	3.130	
	(220)	20.698	790.5	1.917	1.724
	(311)	24.326	849.1	1.635	3.031
Si <sub>H+W</sub> +FSN	(002)*	11.787	445.4	3.355	
	(111)	12.634	624.2	3.130	
	(220)	20.698	451.7	1.917	2.215
	(311)	24.315	455.4	1.636	4.493

**Table 1.** XRD analysis determined structure parameters of  $Si_p + FSN$  and  $Si_{H+W} + FSN$ . \*diffraction peak of FSN (002) facet. \*\* $H_{(111)}/H_{(hkl)}$  denotes the ratio of peak intensities for (111) and (hkl) facets. In an ideal Si crystal with a symmetric group of 227,  $H_{(111)}/H_{(220)}$  is 1.497 and  $H_{(111)}/H_{(311)}$  is 1.794. (source: Materials Project ID: mp-149/, https://doi.org/10.17188/1190959).

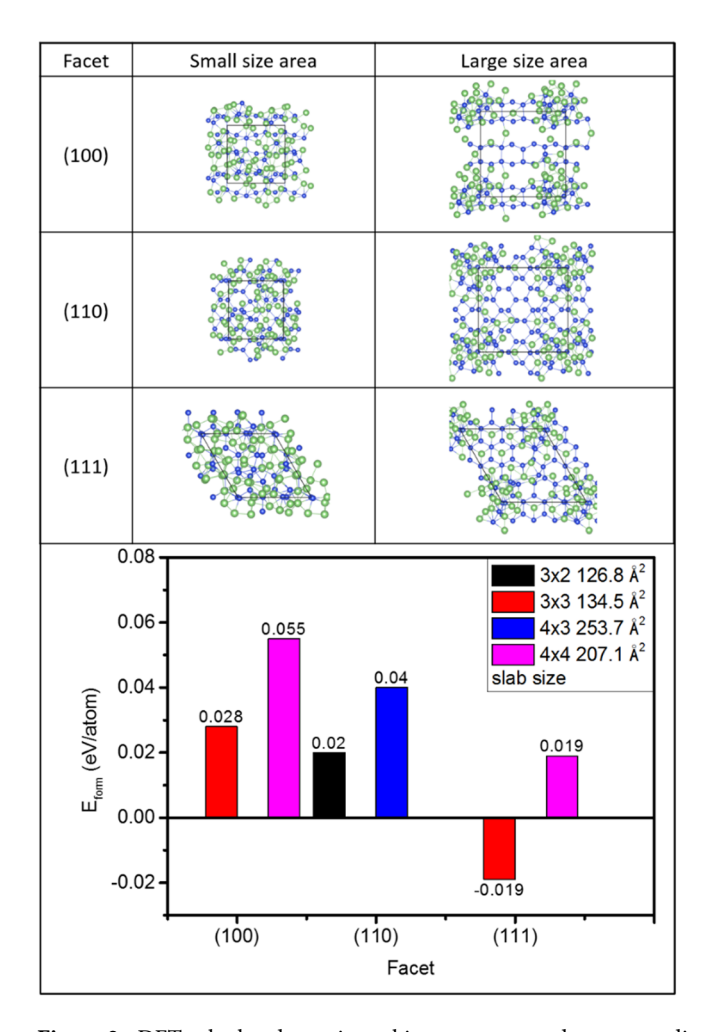


**Figure 2.** DFT calculated atomic packing structure and corresponding formation energy ( $E_{form}$  (eV/atom)) for models comprising two  $Li_{15}Si_4$  clusters in Si slabs surface with facets indexed by the first three diffraction peaks of experimental samples.

slabs and corresponding formation energy ( $E_{form}$  (eV/atom)) with facets indexed by the first three diffraction peaks in Fig. 1. Accordingly, the two  $Li_1sSi_4$  clusters built from its primitive bulk structure (ICSD no.167674) are homogeneously packing on surface with a slab size of 116.5–134.5 Ų. Such a result can be rationalized by steric effects when two  $Li_1sSi_4$  clusters are stacked in a surface with an area smaller than their close packed dimension (cross section area). Formation energies ( $E_{form}$ ) are -0.019 (eV/atom) for (111), 0.02 (eV/atom) for (220), and 0.028 (eV/atom) for (311) facets. A negative value of  $E_{form}$  indicates an exothermic reaction meaning the strong preference of silicide formation in (111) facet when slab size is  $3 \times 3$  (134.5 Ų). As for models with slab sizes of 207.1 to 253.7 Ų,  $E_{form}$  follows the same trend to that of model with small slabs (126.8 to 134.5 Ų). Among them,  $E_{form}$  of (111) is 0.019 (eV/atom). This value is reduced respectively by 52.5% and 65.4% as compared to that of

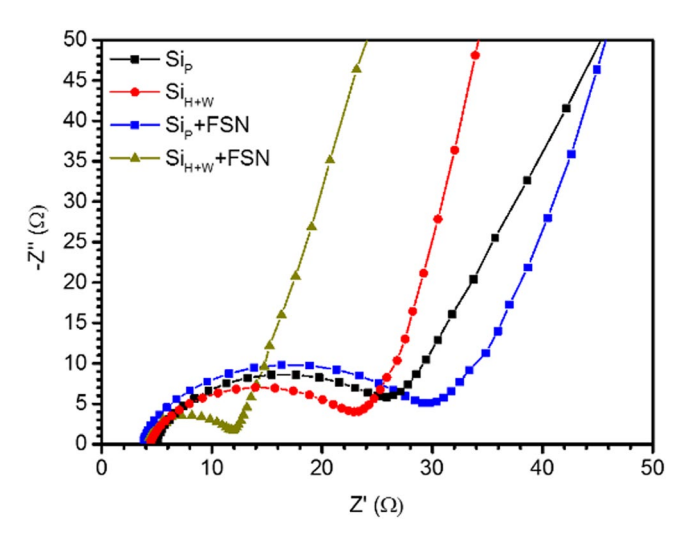


**Figure 3.** Nyquist plots for  $Si_p$ ,  $Si_p + FSN$ ,  $Si_{H+W}$ , and  $Si_{H+W} + FSN$  as negative electrode in as-prepared LIB coin cells.

(220) (0.04, eV/atom) and (311) (0.055, eV/atom) facets again showing a strong preference of silicide formation in (111) facet regardless the presence of steric effects in Si phase interface. Preference of silicide formation is further revealed by the homogeneous distribution of atomic packing scheme in (111) facet. For rest of two facets ((220) and (311)), silicide clusters tend to accumulate in slab corners. Given that accumulation of silicide occurs both in slabs with a large (253.7 Å<sup>2</sup>) and small (207.1 Å<sup>2</sup>) areas, steric effects should be a minor factor in Li silicide formation as compared to facet selectivity (i.e., selectivity of facet) in crystal surface once improper atomic packing configuration is adopted. With proper atomic packing configuration (i.e., (111) facet), E<sub>form</sub> is substantially reduced by 0.038 (eV/atom) with slab size by  $\sim$ 70 Å<sup>2</sup> (from 207.1 to 134.5 Å<sup>2</sup>). Above interpretations could be explained by effects of interface lattice mismatch and atomic arrangements on heterogeneous crystal growth of silicide in a Si crystal surface. For growing polycrystalline thin films on a crystal with completely different structure symmetry, increasing surface atomic packing density reduces local steric barrier for the subsequent position of film atoms. On the other hand, with a large local steric barrier in opened facets (i.e., (220) and (311)) reduction of E<sub>form</sub> with slab size is insignificant and is because of the higher energy for silicide to packing in surface defects. It is surely that presence of surface defects facilitates Li intercalation to growth Li silicide, however, such assessment and effect might lead to side effects (such as electrolyte decomposition and Si oxidation, etc.) and are not the topic to be discussed in this study.

Effects of preferential facet and particle size (predicted by DFT calculation and XRD analysis) on Li intercalation and Li silicide formation are complementary revealed combining electrochemical and operando XRD analysis on LIB with experimental Si materials (Si $_P$  + FSN and Si $_{H+W}$  + FSN) as negative electrode. Figure 3 displays the Nyquist plots of electrochemical impedance spectra (EIS) obtained from experimental Si based negative electrode at 0% lithiated state. These cells exhibited a semicircle in high frequency and a straight line in low frequency ranges, which are attributed to kinetics of charge transfer in interface and Li ions diffusion in bulk electrodes, respectively. As can be seen, a lower electrode impedance of  $\mathrm{Si}_{\mathrm{H+W}}$  indicates its smaller interfacial charge-transfer resistance (Rct) as compared to that of  $Si_P$  Such a phenomenon reveals the facilitation of Li intercalation in  $Si_{H+W}$ surface due to the surface amorphization (probed by HRTEM images), preferential (111) facets, and reduced  $D_{avg}$  (at (220) and (311) facets) in  $Si_{H+W}$ . In a meantime, a uniform and local disordered amorphous Si thin layer (as consistently proved by HRTEM and XRD analyses) is formed in fresh silicon surfaces by wet milling which provides an easy access for Li intercalation. In addition, physical impacts of high energy mechanical milling and wet milling process reduce the primary and agglomerate size which shorten the Li ion diffusion length in a silicon particle. Presence of FSN provide additional Li storage sites. Those Li storage sites share the redox loading and thus reduce chemical stress in Si surface. As denoted by reducing of semicircle diameters, presence of FSN modulates the redox kinetics and thus reduces impedance of Li intercalation in silicon-based electrode.

Internal standard structure labelling on Li affinity of Si based materials. Synchrotron based *operando* XRD analysis further confirms the effects of crystal size, facet selectivity on silicide formation affinity, therefore, projects cyclability of Si materials in LIB. XRD patterns of LIBs containing negative electrodes of  $Si_P + FSN$  and  $Si_{H+W} + FSN$  in the first lithiation/delithation cycle are compared in Fig. 4a,e, respectively. As can been seen, the three peaks at 11.3° (P), 11.8° (Q), and 12.6° (R) are diffraction lines from  $LiC_{12}$  (002), graphite (002) (C (002)), and Si (111) facets. Rest of peaks at 9° and 10.48° are diffraction lines for (211) (peak S) and (220) facets (peak T) of  $Li_{15}Si_4$ . For  $Si_P + FSN$  (Fig. 4a), intensities of diffraction peaks for silicon phase gradually decrease with increasing lithiation ratio to 50%. After that, Si phase is dramatically vanished and  $Li_{15}Si_4$  crystal phase by the end of lithiation. In delithiation process, intensity of peak S and T is decreased indicating a gradual extraction of Li-ions from  $Li_{15}Si_4$ . As consistent revealed in literature, no silicon peaks are found at the end of delithiation process. This phenomenon can be rationalized by formation of amorphous Si due to a severe Li retention. As compared to those of  $Si_P + FSN$ , structure evolutions of Si and silicide phases go even faster in  $Si_{H+W} + FSN$  (Fig. 4e).

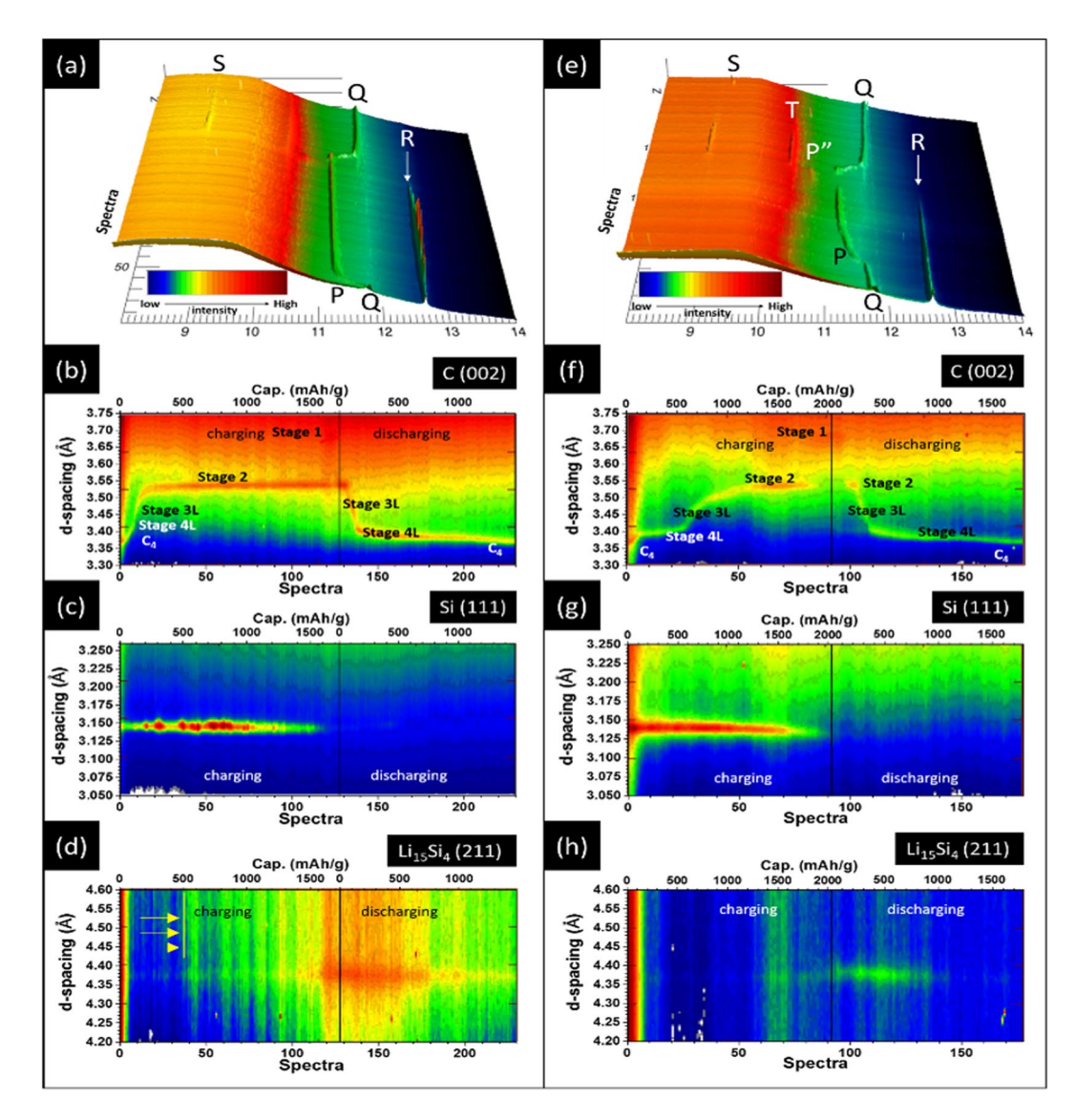


**Figure 4.** *In-situ* XRD patterns (top panel), and changes of  $d_{(002)G}$  (second row),  $d_{(111)Si}$  (third row),  $d_{(211)Li15Si4}$  (bottom row) for  $(\mathbf{a}-\mathbf{d})$  Si<sub>P</sub> + FSN and  $(\mathbf{e}-\mathbf{h})$  Si<sub>H+W</sub> + FSN as negative electrodes in LIBs in the first lithiation and delithiation processes at a rate of C/6.

For clarifying lithiation affinity of  $\mathrm{Si_P} + \mathrm{FSN}$  ( $\mathrm{Si_{H+W}} + \mathrm{FSN}$ ), quantitative results for crystal structure evolution of graphite (C), Si, and  $\mathrm{Li_1SSi_4}$  phases in the first lithiation and delithiation cycle of LIB are cross-referenced in Fig. 4b–d (Fig. 4f–h). In these figures, unit of x-axis is number of diffraction patterns, that of y-axis is d-spacing. Shown in Fig. 4b and Fig. 4f, insertion of Li ions induces a graphite phase transformations in several stages including stage 4L (whose composition is not well defined), stage 3L ( $\mathrm{LiC_{24}}$ ,  $\mathrm{d_{(002)G}} \sim 3.47$  Å), dilute lattice-gas disordered stage 2 ( $\mathrm{LiC_{18}}$ ), stage 2 ( $\mathrm{LiC_{12}}$ ,  $\mathrm{d_{(002)G}} \sim 3.53$  Å), and stage 1 ( $\mathrm{LiC_6}$ ,  $\mathrm{d_{(001)G}} \sim 3.70$  Å) both in  $\mathrm{Si_P} + \mathrm{FSN}$  and  $\mathrm{Si_{H+W}} + \mathrm{FSN^{16}}$ . In those stages, numerals (1, 2, 3, and 4) refer to number of empty layers between each Li-filled layer, and different stage reflects different d-spacing  $\mathrm{^{16}}$ . By cross-referencing changes of d-spacing between crystal structures of graphite and active material, an interesting correlation to the affinity of Si with adopted treatments are revealed in Fig. 4b–d.

Figure 4b shows 2D contour for changes of inter-planar spacing of graphite (002) facet (C (002)) in  $Si_p + FSN$ . As shown, increasing d-spacing at graphite (002) facet ( $d_{(002)G}$ ) from 3.36 Å to 3.52 Å indicates a successive evolution of Li-intercalated LiC<sub>x</sub> to stage 2 phase with capacity from 0 to 150 mAh g<sup>-1</sup> in lithiation process. By increasing capacity to 150 mAh g<sup>-1</sup>,  $d_{(002)G}$  is linearly expanded to that of Li enriched stage (stage 2, LiC<sub>12</sub>). Given that mass ratio of FSN is 50 wt% (equivalent to an ideal capacity of ~170 mAh g<sup>-1</sup>) in active material, transformation of graphite to stage 2 (LiC<sub>12</sub>) suggests that Li ions are mostly intercalate in FSN. In this event, FSN performs a substantial higher affinity for Li intercalation as compared to that of  $Si_p$  in active material. After capacity higher than 150 mAh g<sup>-1</sup>,  $d_{(002)G}$  is slightly increased by 0.01 Å (from 3.52 to 3.53 Å) by a subsequent lithiation to 1720 mAh g<sup>-1</sup>. For structural interpretation in details, changes of peak intensity for Si phases in  $Si_p + FSN$  and  $Si_{H+W} + FSN$  with lithiation ratio are compared in Figs S3a and S3b. Accordingly, with an absence of LiC<sub>6</sub> phase and vibration of Si (111) peak intensity (Fig. 4c), one can notice that most of Li is intercalated in Si phase with lithiation ratios

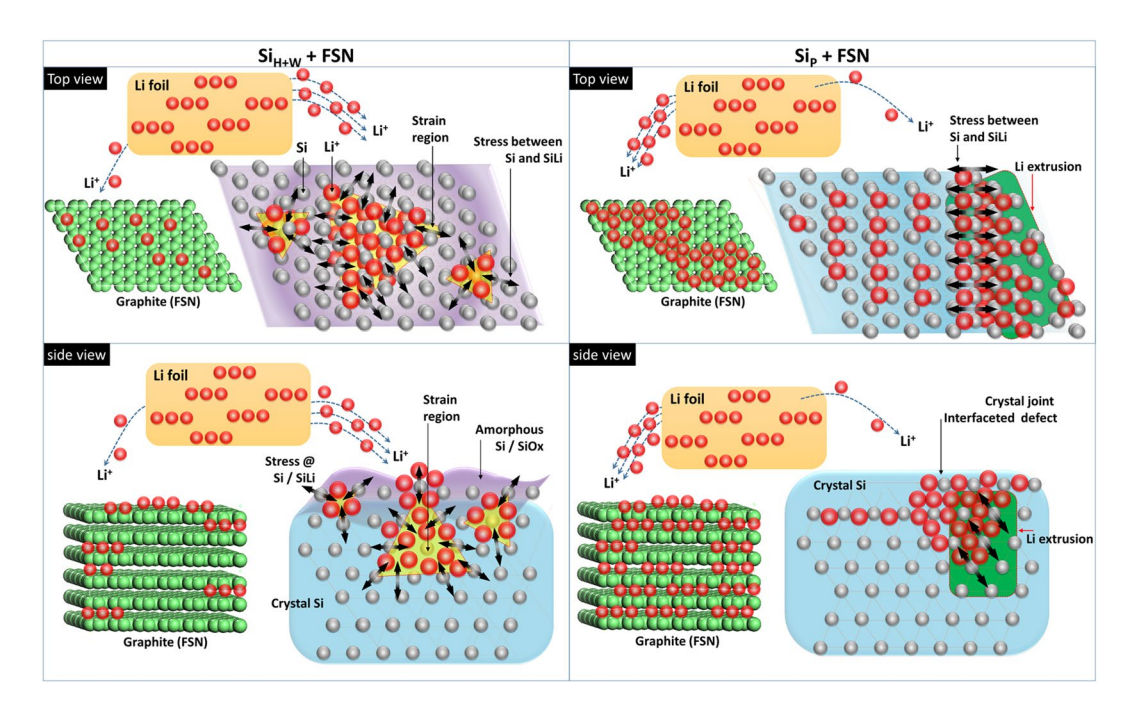


**Figure 5.** Schematic representation to Li intercalation manners in Si materials with  $(Si_{H+W})$  and without  $(Si_P)$  high energy ball milling treatment. Strain regions in amorphous layer possess large local space for Li intercalation and flat surface (i.e., (111) facet) reduce formation energy for Li silicide in Si powder surface. The two pathways facilitate Li intercalation in  $Si_{H+W}$  reducing crack in Si crystal. In  $Si_P$  ratios of open facets (i.e., (220) and (311)) are higher than that in  $Si_{H+W}$ . In open facets, silicide tend to cluster in corner region defect sites to form strong strain. In this event,  $Li^+$  ions would either extrude in bulk or induce a strong interface lattice mismatch to crack Si crystal.

from 15 to 100% in  $Si_p + FSN$  with a capacity of ~1570 mAh  $g^{-1}$ . With a mass ratio of 50 wt% in active materials, this value is decreased by ~18% as compared to theoretical capacity of Si (1850 mAh  $g^{-1}$ ) and is possibly due to a crack of  $Li_vSi$  phases from Si surface in a  $Si_p + FSN$  electrode.

In a  $Si_{H+W}$  + FSN electrode (Fig. 4e), four stages including stage 4L (100–590 mAh g<sup>-1</sup>), 3L (590–1200 mAh  $g^{-1}$ ), stage 2 (1200–1890 mAh  $g^{-1}$ ), and stage 1 (1900–2030 mAh  $g^{-1}$ ) are found in graphite phase evolution by lithiation from 0 to 100% (2030 mAh g<sup>-1</sup>). Among them, stage 1 is fully lithiated graphite phase and can only be formed by a kinetics balance between intercalation and diffusion rates of Li ions in graphite surface in a negative electrode lithiated higher than 94%. It is important to note that active materials possess a higher than 98% of ideal capacity of graphite and Si phases in  $Si_{H+W}$  + FSN; where capacity contribution is ~170–180 mAh  $g^{-1}$  for graphite  $phase\ and\ \sim 1800-1900\ mAh\ g^{-1}\ for\ Si\ phase.\ Compared\ to\ that\ of\ Si_p+FSN,\ graphite\ phase\ delay\ with\ lithiation$ ratio indicates that affinity of Li ion to surface modified Si phase is substantial higher than that of graphite phase in Si<sub>H+W</sub>+FSN. Those scenarios are direct evidences rationalizing the strong lithiation preferential of Si (111), amorphous Si, and defect regions in  $Si_{H+W} + FSN$  electrode. Facile delithiation from  $Si_{H+W} + FSN$  is consistently revealed by phase transition of graphite. Shown in Fig. 4f,  $d_{(002)G}$  hold in stage 1 by delithiation from 0 to 125 mAh  $g^{-1}$  and then move to stage 2 until 235 mAh  $g^{-1}$ . Further delithiation from 235 to 375 mAh  $g^{-1}$  results in a transfer sition from stage 3L to stage 4L in graphite. In this region, this delithiation value is doubled to that can be offered by graphite meaning that Li extraction is mainly from Si phase in a  $Si_{H+W}+FSN$  electrode. On the other hand, in delithiation process of a Si<sub>P</sub> + FSN electrode (Fig. 4b), stage 2 to stage 4L transition is found by delithiation from 0 to 160 mAh g<sup>-1</sup> meaning that most of capacity is contributed from graphite phase (i.e., activation energy for Li extraction from graphite is lower than that from Si phase). Preference of lithiation/delithiation remaining hold even at the  $50^{th}$  cycles and is consistently revealed by comparing changes of  $d_{(002)G}$  between  $Si_P + FSN$  and  $Si_{H+W}$  + FSN with respect to lithiation ratios of LIBs (Fig. S3).

Structure evolutions of Si phases provide complimentary information to the preferential lithiation of active materials in negative electrode of LIB. Shown in Fig. 4g, position of Si(111) peak for Si<sub>P</sub> + FSN remaining unchanged in lithiation process. In this region, intensity of Si(111) peak is vibrating between 200 to 1100 a.u. with increasing capacity to 1490 mAh g<sup>-1</sup> and then dramatically decreased to 0 by a subsequent lithiation till 1570 mAh g<sup>-1</sup> (Fig. S3a). A dramatic vibration of peak intensity implies a crack of Si powder due to a strong lattice mismatch between Li silicide. This hypothesis is proved by presence of wide range scattering signals (denoted by yellow arrows) and diffraction line of Li<sub>15</sub>Si<sub>4</sub> (211) by increasing capacity higher than 500 mAh g<sup>-1</sup> in Fig. 4d. Schematic representation for silicide formation induced interface crack in Si<sub>P</sub> is shown in Fig. 5. For Si<sub>H+W</sub> + FSN, Li<sub>15</sub>Si<sub>4</sub> (211) peak intensity is increased from 0 to 40 a.u. by delithiation from 0 to 500 mAh g<sup>-1</sup> and then progressively decreased to 0 in a subsequent delithiation till 1200 mAh g<sup>-1</sup> (Figs 4h and S3b). As compared to those of in Si<sub>P</sub> + FSN, substantially weakened intensity with a broad width and delayed response of Li<sub>15</sub>Si<sub>4</sub> (211) peak reveal a suppression of Li silicide. Such a characteristic can be attributed to formation of local disordered Si/SiO<sub>x</sub>

and increased ratio of (111) facets dimension with proper interface to facilitate Li intercalation and formation of amorphous Li silicide in  $Si_{H+W}$  + FSN surface (Fig. 1 and Table 1). Effects of HEMM treatments on facilitating Li accommodation in Si surface remaining hold in long-term cycling test till the 50th cycle which again consistently proved the facilitations of silicide formation in (111) facets and reduced D<sub>avg</sub> as predicted by DFT calculation and EIS analysis. Meanwhile, the same scenario on graphite phase evolutions delay proves the substantial improvement of Li intercalation/extraction performances of Si materials even hold after 50 cycles of LIB. Details of graphite evolutions in  $50^{th}$  cycles are given in ESI (Fig. S2) and latter sessions. Rates of  $d_{(002)G}$  to lithiation ratio  $(\Delta d_{(002)G}/\Delta L)$  of negative electrodes are compared Fig. S4 and corresponding peak area (which can be serve as a qualitative index for extent of graphite phase transition) are compared in Table S2 for further revealing the graphite evolution as affected by affinity of Si to Li<sup>+</sup> ions. Shown in Fig. S4a, the four  $\Delta d_{(002)G}/\Delta L$  peaks in (1) 3.9%, (2) 6.8%, (3) 8.1%, and (4) 94.8% of lithiation ratios correspond to the maximum rate for graphite phase transition (i.e., stage 4L, stage 3L, stage 2, and stage 1) in Si<sub>P</sub> + FSN. The first three peaks incur 97.8% of area indicate that most of active sites in graphite phase are lithiated in a lithiation ratio of 8.1% (i.e., ~260 mAh g<sup>-1</sup>) for negative electrode. For the case of  $Si_{H+W}$  + FSN, the  $\Delta d_{(002)G}/\Delta L$  peaks at lithiation ratios of (1) 4.6%, (2) 28.6%, (3) 30.2%, (4) 36.1, and (5) 51.8% suggest the presence of five transient states in graphite phase of Si<sub>H+W</sub> + FSN. In this event, as revealed by area of all  $\Delta d_{(002)G}/\Delta L$  peaks, most active sites (~96.1%) in graphite phase are lithiated in 36.1% of lithiation ( $\sim$ 1240 mAh g $^{-1}$ ) for Si<sub>H+W</sub> + FSN. In a subsequent lithiation, a broad peak across 36.1 to 58.1% can be attributed to formation of LiC<sub>6</sub> transient state. As compared to that of Si<sub>P</sub> + FSN, transition of graphite phases is delayed by 20–25% of lithiation ratio in  $Si_{H+W}$  + FSN. Given that phase transition rate of active materials is dominated by their affinity to Li<sup>+</sup> ion, such a phase delay again consistently revealed the improvement of Li affinity on Si phase in Si<sub>H+W</sub> + FSN. Taking results of operando XRD analyses together, changes of graphite and Si phases with lithiation ratios in the first lithiation step of Si<sub>P</sub> + FSN and Si<sub>H+W</sub> + FSN can be respectively summarized in S4a and S4B. As compared to that of the first cycle, transition of graphite phase is further delayed by ~14 in  $Si_P + FSN$  and  $\sim 10\%$  in  $Si_{H+W} + FSN$ . Such a scenario can be attributed to a reduced lithiation/delithiation barrier by LiSi, formation again proving the concept of graphite phase evolution as internal structural label to Li<sup>+</sup> ion affinity of active materials in LIB.

Crystal structure affinity to formation of Li silicide in long-cycle LIB cells. Quantitative structural parameters on influences of surface modification to cyclability of silicon are determined by fitting the experimental diffraction patterns by the LAMP program. Results of graphite phase evolution (changes of  $d_{(002)G}$ ) with lithiation/delithiation ratios of  $Si_P + FSN$  in the  $1^{st}$  and  $50^{th}$  cycles are shown Fig. S5a. In lithiation process, Li<sup>+</sup> ions move from Li metal to the negative electrodes. In  $Si_P + FSN$ ,  $d_{(002)G}$  is significantly increased to a value of ~3.53 Å by increasing lithiation ratios from 5 to ~15%. Such a value is commonly known as a d-space of fully lithiated graphite (LiC<sub>12</sub>). Without significant differences of Si phase evolution in LIB, such a result suggests a lower diffusion barrier for Li<sup>+</sup> ions in solid electrolyte interface (SEI) and graphite surface as compared to that in Si surface. For the case of  $Si_{H+W}$ , situation goes to the opposite. As shown in Fig. S5b,  $d_{(002)G}$  is increased to that of stage 4L (3.37 Å) by increasing lithiation ratios from 5% to 30%. After that,  $d_{(002)G}$  is then dramatically increased to that of stage 3L (3.47 Å) when ratio of lithiation is 40% and then progressively increased to 3.53 Å (stage 2) till 100%. Hereafter, one can notice a delay of  $d_{(002)G}$  in  $Si_{H+W} + FSN$  as compared to that in  $Si_P + FSN$  in lithiation/delithiation processes. Such a delay on  $d_{(002)G}$  with lithiation extent coincide to an inverse proportional of formation energy of  $Li_{15}Si_4$  in Si surface as consistently proved by DFT calculations.

Changes of  $d_{(002)G}$  with capacity in lithiation and delithiation processes of  $Si_P + FSN$  and  $Si_{H+W} + FSN$  in the  $50^{th}$  cycle are respectively shown in Fig. S6c and S6d. Accordingly, trends of  $d_{(002)G}$  evolutions in  $Si_P + FSN$  in the  $50^{th}$  cycle is differed from that in the  $1^{st}$  cycle. Shown in Fig. S6c, changes of  $d_{(002)G}$  in  $Si_P + FSN$  is significantly retarded in the 50th delithiation process as compared to that in the 1st delithiation process. Such a delayed response on graphite phase and be explained by formation of significant amount of amorphous Si and retained Li silicide (i.e., irreversible capacity) in Si<sub>p</sub> + FSN in long-cycle test. Meanwhile, as consistently explained by vibration of Si(111) peak intensity, loss of capacity reveals a crack (pulverization) of Si particle in Si<sub>P</sub> + FSN in long cycle test which increases internal resistance between Si phases and back contact electrode. Changes of  $d_{(002)}$  $_{\rm G}$  for Si<sub>P</sub> + FSN and Si<sub>H+W</sub> + FSN in delithiation process are compared in Fig. S6d. As depicted, Si<sub>P</sub> + FSN and Si<sub>H+W</sub> + FSN perform a similar decay trend on d<sub>(002)G</sub>. It means that graphite phase possesses a similar energy barrier for Li intercalation in both the two electrodes in the 50<sup>th</sup> delithiation process. It is worth to note that, as compared to that of  $Si_{H+W} + FSN$  in the  $1^{st}$  cycle,  $d_{(002)G}$  is suspended in stage IV by further increasing delithiation by 8–9%. It rationalizes the Li intercalation in Si phase is further facilitated in the  $50^{th}$  cycle for  $Si_{H+W} + FSN$  in a LIB. Those results prove that formation of surface amorphous Si layer and increase ratio of (111) facet domain size with local distortion and surface modification by HEMM treatments improve the affinity of Li intercalation and extraction in Si surface (Fig. 5). Such a method is easy assessable therefore promising the development of Si based materials in LIB applications.

Cycle performance test further confirms the prediction on cyclability of Si materials by *operando* XRD analysis. Figure 6 shows the (a) specific capacity and (b) charging capacity retention (CR) of Si<sub>p</sub>, Si<sub>p</sub> + FSN, Si<sub>H+W</sub> and Si<sub>H+W</sub> + FSN negative electrodes in LIBs till the 50<sup>th</sup> lithiation/delithiation cycle. In the cycle test, rate is C/6 and potential range is 2 mV to 1.5 V. Accordingly, Si<sub>p</sub> possesses a capacity of 3236 mAh g<sup>-1</sup> in lithiation process and 2655 mAh g<sup>-1</sup> in delithiation process in the 1<sup>st</sup> cycle (formation stage). For Si<sub>H+W</sub>, capacity is 3470 mAh g<sup>-1</sup> in lithiation and 2845 mAh g<sup>-1</sup> in delithiation processes. It is important to note that both the Si<sub>p</sub> and Si<sub>H+W</sub> perform a columbic efficiency of ~82% in formation stage, however, with completely different fading manners of CR fading in a cycle test. For Si<sub>p</sub> CR is exponentially decreased to 10% till the 50<sup>th</sup> cycle. On the other hand, CR is decreases by ~15% in the first five cycles (region A) and then slightly decreased by ~4% in the subsequent cycles (region B) for Si<sub>H+W</sub>. As compared to that of Si<sub>p</sub> a substantially reduced CR decay in region A implies a reduction of energy barrier for silicide formation therefore improving cycle stability of Si<sub>H+W</sub>.

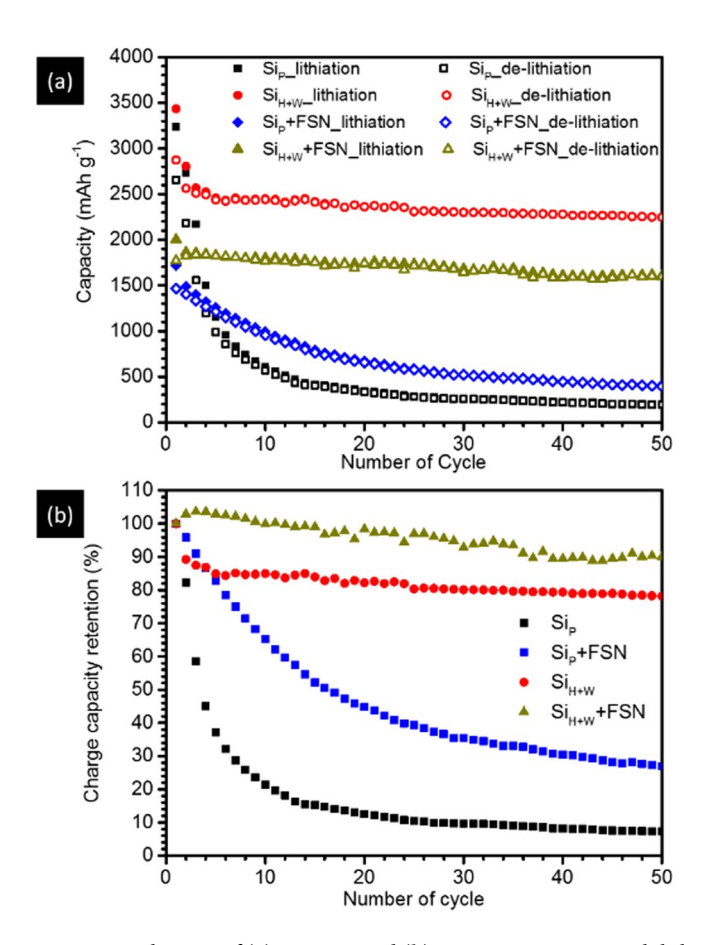


**Figure 6.** Changes of (a) capacity and (b) capacity retention with lithiation/delithiation cycles of LIBs equipped with  $Si_p$ ,  $Si_p + FSN$ ,  $Si_{H+W}$ , and  $Si_{H+W} + FSN$  negative electrodes. In these tests, rate is C/6 and potential is ranged between 0.02 V and 1.5 V vs. Li/Li<sup>+</sup>.

Addition of conducting graphite (FSN) further enhances the difference of capacity fading mode between  $\mathrm{Si}_P$  and  $\mathrm{Si}_{H+W}$ . Show in Fig. 6b, fading rate of  $\mathrm{Si}_P$  is substantially reduced by mixing FSN in a weight ratio of FSN/  $\mathrm{Si}_P=1.0$ . Although capacity fading is improved by 19.6%, its CR fading remaining reaction control. On the other hand, CR fading of  $\mathrm{Si}_{H+W}$  shows the opposite way to that of  $\mathrm{Si}_P$  when mixing with FSN in the same weight ratio. In the  $2^{nd}$  cycle, a slight increase of capacity might be attributed to the excess Li storage in FSN as compared to that of the  $1^{st}$  cycle. Such a hypothesis is further revealed by results of operando XRD analysis and impedance test which proving the insufficient/uncompleted Li intercalation in FSN in the first lithiation process. Similar to that of  $\mathrm{Si}_P$  CR fading of  $\mathrm{Si}_{H+W}$  is improved by 12% by FSN additive with cycle number to 50.

# **Conclusions**

Graphite phase evolution is employed to evaluate cyclability of Si based materials as negative electrode in an operando LIB cell. At the first cycle, delay of  $d_{(002)G}$  expansion with increasing capacity reveals a strong preference of Li ion intercalation in silicon phase in negative electrode of  $Si_{H+W}+FSN$  comprising modified Si powder in lithiation process. As compared to that of  $Si_{H+W}+FSN$ ,  $d_{(002)G}$  is linearly increased and stabled to that of fully lithiated graphite (3.53 Å) with respect to a capacity of ~170–180 mAh g<sup>-1</sup> revealing that Li<sup>+</sup> ions are mostly intercalated in graphite phase by lithiation to 5% in negative electrode of  $Si_P+FSN$  comprising pristine Si powder. Those scenarios are further confirmed by cross-referencing results of XRD, HRTEM, and DFT calculation indicating that performance of Si materials are improved by formation of preferential (111) facet accompanied with certain amorphous structure by HEMM treatment. A most important finding is that  $d_{(002)G}$  delay remaining hold in an operando LIB cell even in the 50<sup>th</sup> lithiation/delithiation cycle. Such a scenario, in a fact of phase evolution dominated by Li interaction, proves that changes of  $d_{(002)G}$  with lithiation ratios is a robust qualitative index for predicting the cyclability of active materials in the formation stage of a LIB.

## Methods

Experimental details - Sample preparation, LIB assembly, and Physical Structure Characterizations. Commercial silicon powder was purchased from Fuzhou Hokin Chemical Technology, China (Si<sub>P</sub> ~10 um). To modify surface conformation of Si<sub>P</sub> high energy mechanical milling (HEMM) and wet ball-milling in a planetary miller for 20 hours at room temperature were employed and resulting product is named as Si<sub>H+W</sub> <sup>15</sup>. Artificial graphite (FSN, Shanshan Technology, China, ~15 um) was employed as an internal structure standard for labelling lithiation and delithiation affinity of active materials in negative electrode of LIB. The

electrochemical measurements and the investigations of structural evolution of the silicon/graphite composite electrode were carried out by using CR2032 coin-cells. Experimental negative electrodes were prepared by casting 15  $\mu$ m of active materials mixture in aluminium foil. The mixture contains 65 wt% of active materials (mixture of Si<sub>P</sub> and Si<sub>H+W</sub> respectively with FSN at a weight ratio of silicon/graphite = 1, namely Si<sub>P</sub> + FSN and Si<sub>H+W</sub> + FSN), 20 wt% of carbon black (Super P), 9 wt% of poly(acrylic acid) (PAA, SigmaAldrich Co.), 3.5 wt% of styrene butadiene rubber (SBR, Zeon Co.), and 2 wt% of carboxymethylcellulose (CMC) dissolved in deionized water. Cells were assembled inside an Ar-filled glovebox. In a coin cell, counter (reference) electrode is lithium metal foil and separator is micro-porous polypropylene. The electrolyte was 1 M LiPF<sub>6</sub> solution in a mixture of EC and DMC (1:1 in volume ratio). After assembly, experimental coin cells were stored for two days prior to electrochemical test. Electrochemical impedance spectroscopy (EIS) is employed to investigate the charge transfer resistance and the electronic resistance of activated material in lithium ion batteries. In this study, EIS characterization were performed on coin cells at open-circuit voltage ( $O_{CV}$ ) and the frequency was swept from 1 MHz to 10 mHz.

Operando XRD analysis on experimental coin cells was conducted at Taiwan beamline (BL12B2) of Spring-8 (Aioi, Japan). XRD patterns are measured with an incident x-ray wavelength of 0.688992 Å by an area detector. Pixel resolution of detector equivalents to a step size of  $\sim 0.015^{\circ}$  in two-theta and covers a range from 0 to 30°. The system temperature is  $\sim 30^{\circ}$ C and exposure time is  $3\sim 4$  min per pattern in transmission mode. During the data collection, the operation voltage of LIB is ranged from 2 mV to 1.5 V at a constant current (CC) of  $\sim 0.5$  mA (i.e., at a rate of C/6). For conducting *operando* XRD analysis, one hole is punched and is covered with Kapton film on both top and bottom of case as X-ray window.

Computational details. All calculations were performed in the framework of density functional theory, as implemented in the Vienna Ab initio Simulation Package<sup>17</sup> code within the projected augmented wave (PAW) approach<sup>18</sup>. The Perdew-Burke-Ernzerhof form of the generalized gradient correction (GGA-PBE) functional is used to describe the exchange-correlation interaction <sup>19</sup>. The cutoff energy of 370 eV and Monkhorst-Pack k-point sampling of  $12 \times 12 \times 12$  were employed in Si bulk structure optimization, which were sufficient to obtain converged total energies. The calculated bulk lattice constant of 5.468 Å is consistent with experimental value of 5.431 Å. We utilized large slabs of Si(100) – 12L, Si(110)-8L, and Si(111)-8L to simulate silicon surfaces. The bottom two layers were fixed in its bulk structure and the dangling bonds were saturated by hydrogen atoms, all the rest atoms were optimized with the convergence threshold for energy is 10-5 eV which could provide sufficient accuracy. A vacuum larger than 12 Å is used to avoid the interaction between periodic images. To clarify the affinity of Li silicide on Si surface, we performed analyses of Li<sub>15</sub>Si<sub>4</sub> (most highly lithiated phases) on a series of Si surfaces with different size of area. The structure of Li<sub>15</sub>Si<sub>4</sub> primitive cell consisting of thirty Li atoms and eight Si atoms is available in Inorganic Crystal Structure Database (ICSD, #167674)<sup>20</sup> by utilizing database from Material Project<sup>21</sup>. The formation energy can be obtained from the formula:  $E_{\text{form}} = (E_{\text{total}} - E_{\text{surface}} - \Sigma N_i \mu_i)/N_i$ , where  $E_{\text{total}}$ and E<sub>surface</sub> are the total energies of Li@Si and Si bare surface, respectively. Ni and  $\mu$ i are atom number and chemical potential of species i (Li and Si). Here, we used bulk energy per atom as the chemical potential.

#### References

- 1. Chan, C. K. et al. High-performance lithium battery anodes using silicon nanowires. Nat Nano 3, 31–35, http://www.nature.com/nnano/journal/v3/n1/suppinfo/nnano.2007.411\_S1.html (2008).
- Obrovac, M. N. & Christensen, L. Structural Changes in Silicon Anodes during Lithium Insertion/Extraction. Electrochemical and Solid-State Letters 7, A93–A96, https://doi.org/10.1149/1.1652421 (2004).
- Zhang, J. et al. High-Columbic-Efficiency Lithium Battery Based on Silicon Particle Materials. Nanoscale Research Letters 10, 395, https://doi.org/10.1186/s11671-015-1103-0 (2015).
- 4. Lee, S. W., McDowell, M. T., Berla, L. A., Nix, W. D. & Cui, Y. Fracture of crystalline silicon nanopillars during electrochemical lithium insertion. *Proceedings of the National Academy of Sciences* 109, 4080–4085, https://doi.org/10.1073/pnas.1201088109 (2012).
- Su, X. et al. Silicon-Based Nanomaterials for Lithium-Ion Batteries: A Review. Advanced Energy Materials 4, n/a-n/a, https://doi. org/10.1002/aenm.201300882 (2014).
- Xu, C. et al. Improved Performance of the Silicon Anode for Li-Ion Batteries: Understanding the Surface Modification Mechanism
  of Fluoroethylene Carbonate as an Effective Electrolyte Additive. Chemistry of Materials 27, 2591–2599, https://doi.org/10.1021/acs.
  chemmater.5b00339 (2015).
- 7. Kasavajjula, U., Wang, C. S. & Appleby, A. J. Nano- and bulk-silicon-based insertion anodes for lithium-ion secondary cells. *J. Power Sources* 163, 1003–1039, https://doi.org/10.1016/j.jpowsour.2006.09.084 (2007).
- 8. Li, H. et al. The crystal structural evolution of nano-Si anode caused by lithium insertion and extraction at room temperature. Solid State Ionics 135, 181–191, https://doi.org/10.1016/s0167-2738(00)00362-3 (2000).
- 9. Si, Q. et al. A high performance silicon/carbon composite anode with carbon nanofiber for lithium-ion batteries. *J. Power Sources* 195, 1720–1725, https://doi.org/10.1016/j.jpowsour.2009.09.073 (2010).
- Liu, X. H. et al. Size-Dependent Fracture of Silicon Nanoparticles During Lithiation. ACS Nano 6, 1522–1531, https://doi. org/10.1021/nn204476h (2012).
- 11. Yao, Y., Liu, N., McDowell, M. T., Pasta, M. & Cui, Y. Improving the cycling stability of silicon nanowire anodes with conducting polymer coatings. *Energy & Environmental Science* 5, 7927–7930, https://doi.org/10.1039/C2EE21437G (2012).
- Zhou, X., Yin, Y.-X., Cao, A.-M., Wan, L.-J. & Guo, Y.-G. Efficient 3D Conducting Networks Built by Graphene Sheets and Carbon Nanoparticles for High-Performance Silicon Anode. ACS Applied Materials & Interfaces 4, 2824–2828, https://doi.org/10.1021/am3005576 (2012).
- Ko, M., Chae, S. & Cho, J. Challenges in Accommodating Volume Change of Si Anodes for Li-Ion Batteries. ChemElectroChem 2, 1645–1651, https://doi.org/10.1002/celc.201500254 (2015).
- 14. Chockla, A. M. et al. Silicon Nanowire Fabric as a Lithium Ion Battery Electrode Material. *Journal of the American Chemical Society* 133, 20914–20921, https://doi.org/10.1021/ja208232h (2011).
- 15. Hou, S.-C. *et al.* The synergistic effects of combining the high energy mechanical milling and wet milling on Si negative electrode materials for lithium ion battery. *Journal of Power Sources* 349, 111–120, https://doi.org/10.1016/j.jpowsour.2017.03.024 (2017).
- Flandrois, S. & Simon, B. Carbon materials for lithium-ion rechargeable batteries. Carbon 37, 165–180, https://doi.org/10.1016/ S0008-6223 (1999).
- 17. Kresse, G. & Furthmüller, J. Efficient iterative schemes for ab initio total-energy calculations using a plane-wave basis set. *Physical Review B* **54**, 11169–11186 (1996).

- 18. Blöchl, P. E. Projector augmented-wave method. Physical Review B 50, 17953-17979 (1994).
- 19. Perdew, J. P., Burke, K. & Ernzerhof, M. Generalized Gradient Approximation Made Simple [Phys. Rev. Lett. 77, 3865 (1996)]. *Physical Review Letters* **78**, 1396-1396 (1997).
- Bergerhoff, G., Hundt, R., Sievers, R. & Brown, I. D. The inorganic crystal structure data base. *Journal of Chemical Information and Computer Sciences* 23, 66–69, https://doi.org/10.1021/ci00038a003 (1983).
- Kubota, Y., Sison Escano, M. C., Nakanishi, H. & Kasai, H. Crystal and electronic structure of Li<sub>15</sub> Si<sub>4</sub>. Journal of Applied Physics 102, 053704-053701-053704-053706 (2007).

# **Acknowledgements**

The authors thank the help by staffs of National Synchrotron Radiation Research Center (NSRRC), Hsinchu, Taiwan for helping in various synchrotron-based measurements. The VASP based DFT calculation and the results were conducted by using the clusters at National Center for High-Performance Computing (NCHC), Taiwan. T.-Y. Chen thanks the funding support from the Ministry of Science and Technology, Taiwan (MOST 106-2112-M-007-016-MY3 and MOST 105-3113-E-006-019-CC2).

## **Author Contributions**

C.-W.H. analyzed the *in-situ* XRD data, J.-P.C. and A.H. performed the DFT calculations, S.-C.H. and W.-K.L. prepared Si powder sample, Y.-F.S. analyzed battery electrochemical properties, T.-Y.C. analyzed *in-situ* data and wrote the manuscript, Y.-F.L. and J.-M.C. installed XRD tool, J.-L.H. evaluated Si powder quality, C.-C.C. evaluated battery bath characterization.

#### Additional Information

**Supplementary information** accompanies this paper at https://doi.org/10.1038/s41598-018-38112-2.

**Competing Interests:** The authors declare no competing interests.

**Publisher's note:** Springer Nature remains neutral with regard to jurisdictional claims in published maps and institutional affiliations.

Open Access This article is licensed under a Creative Commons Attribution 4.0 International License, which permits use, sharing, adaptation, distribution and reproduction in any medium or format, as long as you give appropriate credit to the original author(s) and the source, provide a link to the Creative Commons license, and indicate if changes were made. The images or other third party material in this article are included in the article's Creative Commons license, unless indicated otherwise in a credit line to the material. If material is not included in the article's Creative Commons license and your intended use is not permitted by statutory regulation or exceeds the permitted use, you will need to obtain permission directly from the copyright holder. To view a copy of this license, visit <a href="https://creativecommons.org/licenses/by/4.0/">https://creativecommons.org/licenses/by/4.0/</a>.

© The Author(s) 2019